



Cite this: *RSC Adv.*, 2020, 10, 19474

Wide visible-range fluorescence of Eu^{3+} located in the macroscopic bi-layer ceramic/glass composite

Haifeng Shi,^a Jiaxin Yang,^a Zhimin Yu,^a Yu Song,^a Edwin Yue Bun Pun,^b Xin Zhao^{*a} and Hai Lin ^{*ab}

The Eu^{3+} doped fluoride bi-layer ceramic/glass composite ($\text{GC}_{\text{ZBL}}\text{-Eu}$) was prepared by a one-step method and the effective wide visible-range fluorescence was recorded. The de-population rates of the $^5\text{D}_0$, $^5\text{D}_1$, $^5\text{D}_2$, and $^5\text{D}_3$ multi-levels in the glass layer ($\text{G}_{\text{ZBL}}\text{-Eu}$) were estimated to be 214, 746, 1163, and 680 s^{-1} , respectively, and that in the ceramic layer ($\text{C}_{\text{ZBL}}\text{-Eu}$) were 211, 730, 1075, and 654 s^{-1} , which implies multi-channel radiative transitions due to the non-radiative relaxation limitation of low OH content and low phonon energy. Simultaneously, the quantum efficiencies of the $^5\text{D}_0$ levels in $\text{G}_{\text{ZBL}}\text{-Eu}$ and $\text{C}_{\text{ZBL}}\text{-Eu}$ were as high as 98.5% and 94.8%, respectively, thus demonstrating the effectiveness of the radiative transition emissions from Eu^{3+} . Besides, $\text{GC}_{\text{ZBL}}\text{-Eu}$ with the glass forming layer increases the emission intensity by 24% compared to $\text{C}_{\text{ZBL}}\text{-Eu}$, which is attributed to the multiple-cycle reflection in the composite structure of the glass–ceramic transition region, and the color coordinates of $\text{C}_{\text{ZBL}}\text{-Eu}$ (0.483, 0.385) and $\text{GC}_{\text{ZBL}}\text{-Eu}$ (0.469, 0.389) show that they can release yellowish-white light. The hetero-structured $\text{GC}_{\text{ZBL}}\text{-Eu}$ provides a new approach for laser lighting, fluorescent display, and up-conversion applications.

Received 8th February 2020

Accepted 6th May 2020

DOI: 10.1039/d0ra01236j

rsc.li/rsc-advances

Introduction

White light-emitting diodes (WLEDs) have recently attracted considerable attention as next generation light sources and as alternatives for conventional incandescent and fluorescent lamps.^{1–4} One of the most popular ways to obtain WLEDs is to combine near UV-LEDs with a glass or crystal phosphor emitting in the blue, green, and red spectral regions.^{5–7} For this purpose, multiple luminescence centers in the phosphors are widely adopted to achieve high brightness and high color rendering index of white light emission.^{8–12} However, rare earth (RE) co-doping leads to complex cross relaxation processes, which cannot release photons efficiently. In view of the high fluorescence quantum efficiency in visible white light illumination, the exploration focusing on the compound material with single RE^{3+} ions doping and multi-channel emission becomes urgent.

The emission spectrum of Eu^{3+} located in the hosts, characterized by the existence of high energy phonons such as the oxides, is strong only for the case of the bands produced by the radiative relaxations from $^5\text{D}_0$.^{13–19} The emissions from $^5\text{D}_0$ are favored mostly because the energy difference between the $^5\text{D}_3$, $^5\text{D}_2$, $^5\text{D}_1$, and $^5\text{D}_0$ levels of the Eu^{3+} cation can be covered by

non-radiative transitions from the higher levels to $^5\text{D}_0$. The resulting emission profile, with intense bands mostly confined to a narrow range, is not suitable for the preparation of white-light phosphors if the intention is to use only a single RE^{3+} dopant. However, in hosts having weak phonons, such as fluorides, the non-radiative transitions from the higher electronic levels to $^5\text{D}_0$ become difficult and the electronic transitions originating in those levels acquire higher intensity than in the oxide hosts. The result is a fluorescence spectrum exhibiting bands of significant intensity (albeit emission at wavelength higher than 500 nm remains strongest) at various positions of the visible range; such a spectral profile makes Eu^{3+} , in fluorides, a possible candidate for the fabrication of white light phosphors based on a single RE^{3+} . In this work, for the first time, it has been examined whether the emission of Eu^{3+} , introduced in a Zr–Ba–La–F host (macroscopic ceramic/glass bi-layer), can be used to obtain such phosphors. In addition, the transitions $^5\text{D}_0 \rightarrow ^7\text{F}_1$ and $^5\text{D}_0 \rightarrow ^7\text{F}_2$ have different dependences on the crystal field environment belonging to the magnetic dipole and electric dipole transitions.^{20–25} Also, Eu^{3+} ions have similar ionic radius and crystalline properties as other RE^{3+} ions, which can be used as a probe of the local structure to explore the influence of the micro-environment of RE^{3+} ions on the luminescence of materials.

In this work, Eu^{3+} -doped fluoride ceramics with a glass layer ($\text{GC}_{\text{ZBL}}\text{-Eu}$) have been prepared and intense yellowish-white fluorescence, attributed to multi-peak emission, was observed.

^aSchool of Textile and Material Engineering, Dalian Polytechnic University, Dalian 116034, P. R. China. E-mail: zhaoxin@dlpu.edu.cn; lhais8686@yahoo.com

^bDepartment of Electronical Engineering and State Key Laboratory of Terahertz and Millimeter Waves, City University of Hong Kong, Tat Chee Avenue, Kowloon, Hong Kong, P. R. China


With the formation of the thin glass layer on the ceramic surface, the $GC_{ZBL}\text{-Eu}$ increases its emission intensity by 24% compared to $C_{ZBL}\text{-Eu}$, which is ascribed to multiple-cycle reflection in the complex structure of the glass-ceramic transition region. The micro-environment symmetry of $G_{ZBL}\text{-Eu}$ and $C_{ZBL}\text{-Eu}$ is judged according to the value of the J-O parameter Ω_2 with different emission intensity ratios between $^5D_0 \rightarrow ^7F_2$ and $^5D_0 \rightarrow ^7F_1$. The differential fluorescence characteristics, such as the radiative lifetimes of the multi-levels and the quantum efficiency of the 5D_0 levels from Eu^{3+} in $G_{ZBL}\text{-Eu}$ and $C_{ZBL}\text{-Eu}$, were analyzed. In addition, the color coordinates of $C_{ZBL}\text{-Eu}$ and $GC_{ZBL}\text{-Eu}$ are located in the yellowish-white lighting region, which indicates that the hetero-structured materials can be well applied to optical devices.

Preparation and measurements of $GC_{ZBL}\text{-Eu}$

The fluoride bi-layer ceramic/glass composites were prepared according to the molar host composition of $60\text{ZrF}_4\text{-}30\text{BaF}_2\text{-}10\text{LaF}_3$ (ZBL) via the melt-quench method and 0.2 wt% EuF_3 was introduced into the ZBL matrix as the dopant. The well-mixed high-purity fluoride raw materials were melted at 900°C for 5 min in a platinum crucible using an electric furnace at the rate of 5°C min^{-1} from room temperature to 900°C . In addition, NH_4F on the raw materials provides a reducing atmosphere and thus, the molten glass was quenched onto an aluminum plate. Herein, the bottom molten glass, when in contact with the aluminum plate, takes away a lot of heat rapidly and forms an ultrathin glass layer owing to the process of efficient heat conduction. Correspondingly, the upper liquid starts to crystallize at the interface with air because air cannot take away a lot of heat. Subsequently, the molded samples were annealed at 260°C for 2 h and then cooled down slowly to room temperature. The schematic diagram of the systematic preparation procedure is exhibited in Fig. 1. Relevant tests were performed on the glass surface of the bi-layer ceramic/glass composite, the ceramic layer, and the glass layer, which were named as $GC_{ZBL}\text{-Eu}$

Eu , $C_{ZBL}\text{-Eu}$, and $G_{ZBL}\text{-Eu}$, respectively ($C_{ZBL}\text{-Eu}$ and $G_{ZBL}\text{-Eu}$ samples were ground to the glass or ceramic layer by the $GC_{ZBL}\text{-Eu}$ composite).

The differential thermal analysis (DTA) scan was carried out on a WCR-2D differential thermal analyzer at the rate of $10^\circ\text{C min}^{-1}$ from room temperature to 900°C . X-ray diffraction (XRD) measurements for the powders of $G_{ZBL}\text{-Eu}$ and $C_{ZBL}\text{-Eu}$ were carried out on a Shimadzu XRD-7000 diffractometer (40 kV, 30 mA). The morphological behavior of the section of $GC_{ZBL}\text{-Eu}$ was observed by a field-emission scanning electron microscope (SEM instrument, JEOL JSM-7800F). The glass layer thickness of

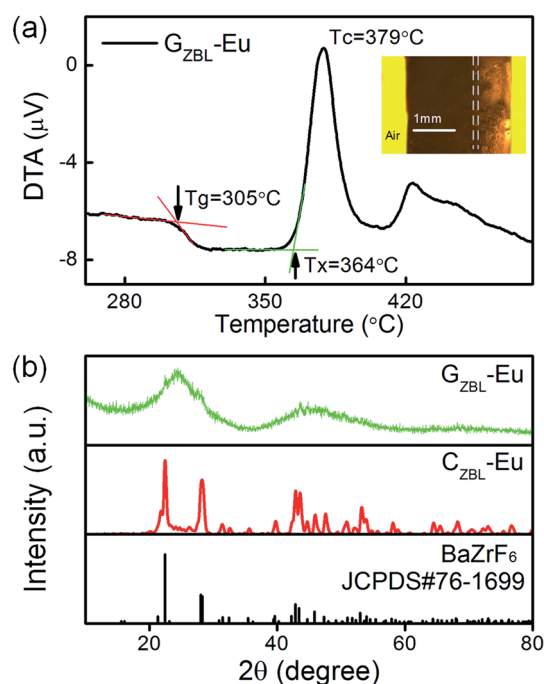


Fig. 2 (a) The DTA curve of $G_{ZBL}\text{-Eu}$. Inset: the cross-section morphology of the $GC_{ZBL}\text{-Eu}$ sample under an optical microscope. (b) The XRD patterns of $G_{ZBL}\text{-Eu}$ and $C_{ZBL}\text{-Eu}$.

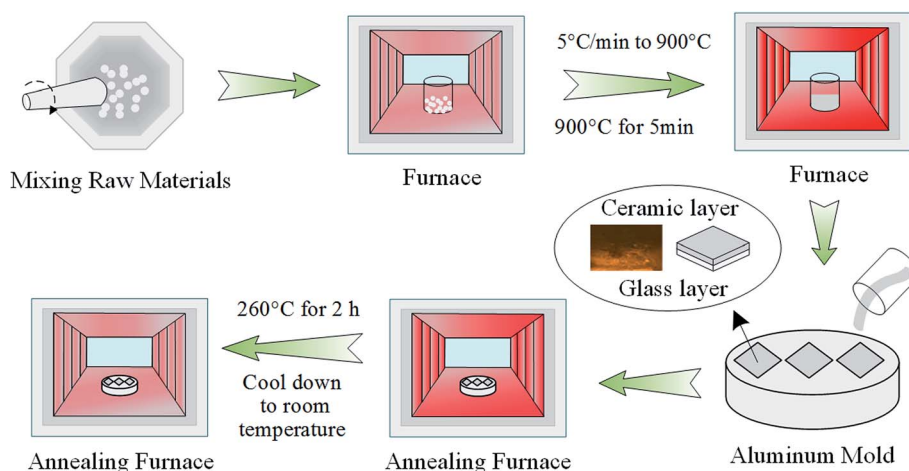


Fig. 1 The schematic diagram of the systematic preparation procedure.

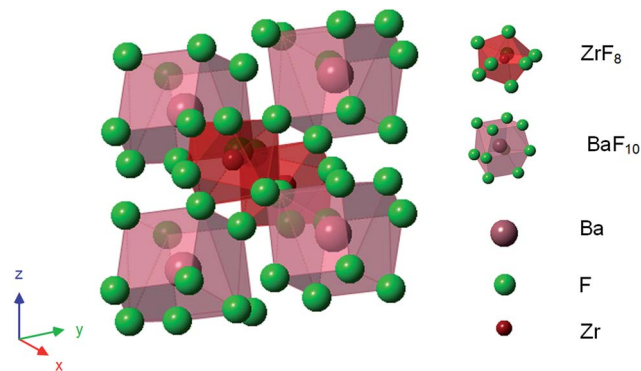


Fig. 3 The schematic illustration of the crystal structure of BaZrF₆.

GC_{ZBL}-Eu was measured by a fluorescence microscope (Imaging system CK-500). The refractive index of G_{ZBL}-Eu was measured by using the Metricon 2010 prism coupler. The visible fluorescence spectra and the fluorescence decay curves were obtained using a Hitachi F-7000 fluorescence spectrophotometer equipped with an R928 photomultiplier tube (PMT) as the detector and a commercial Xe-lamp as the excitation source.

Results and discussion

The transition temperature $T_g = 305$ °C, the onset crystallization temperature $T_x = 364$ °C, and the peak temperature $T_c =$

379 °C of the DTA curve are shown in Fig. 1(a). The parameters including the temperature difference value $\Delta T = T_x - T_g = 59$ °C, the thermal stability parameter $H = \Delta T/T_g = 0.19$, and the Saad-Poulain criterion $S = \Delta T(T_c - T_x)/T_g = 2.9$ °C demonstrate that this sample is more effortless to crystallize than other oxide glasses or oxyfluoride glasses, and is suitable for the preparation of the fluoride ceramic-based composite glass. The inset of Fig. 2(a) shows the cross-sectional morphology of GC_{ZBL}-Eu under an optical microscope. The shiny part of this picture is the glass layer, whose thickness was identified to be ~ 0.81 mm, the dark part is ceramic-based, and the intersection part of the two layers is called the GC transition region.

The typical XRD pattern of G_{ZBL}-Eu in Fig. 2(b) exhibits a broad diffuse scattering at lower angles without the narrow diffraction peaks of the crystal phase and the amorphous state of the prepared glass layer is well-identified. At the same time, by comparing the sharp diffraction peaks in the XRD spectrum of C_{ZBL}-Eu, the crystal phase of C_{ZBL}-Eu is identified to be pure BaZrF₆. The slight differences in the cell parameters between C_{ZBL}-Eu ($a = 7.744$ Å, $b = 11.691$ Å, $c = 5.404$ Å, $\alpha = \beta = \gamma = 90^\circ$) and the standard BaZrF₆ phase ($a = 7.681$ Å, $b = 11.357$ Å, $c = 5.511$ Å, $\alpha = \beta = \gamma = 90^\circ$) indicate the possibility of lattice deformation caused by the introduction of Eu³⁺. The cell volumes of orthorhombic C_{ZBL}-Eu and BaZrF₆ judged by the cell parameters were calculated to be 489.25 and 480.74 Å³ by the equation $V = a \times b \times c$, indicating that the doping of Eu³⁺ has little effect on the cell volume before and after substitution. In

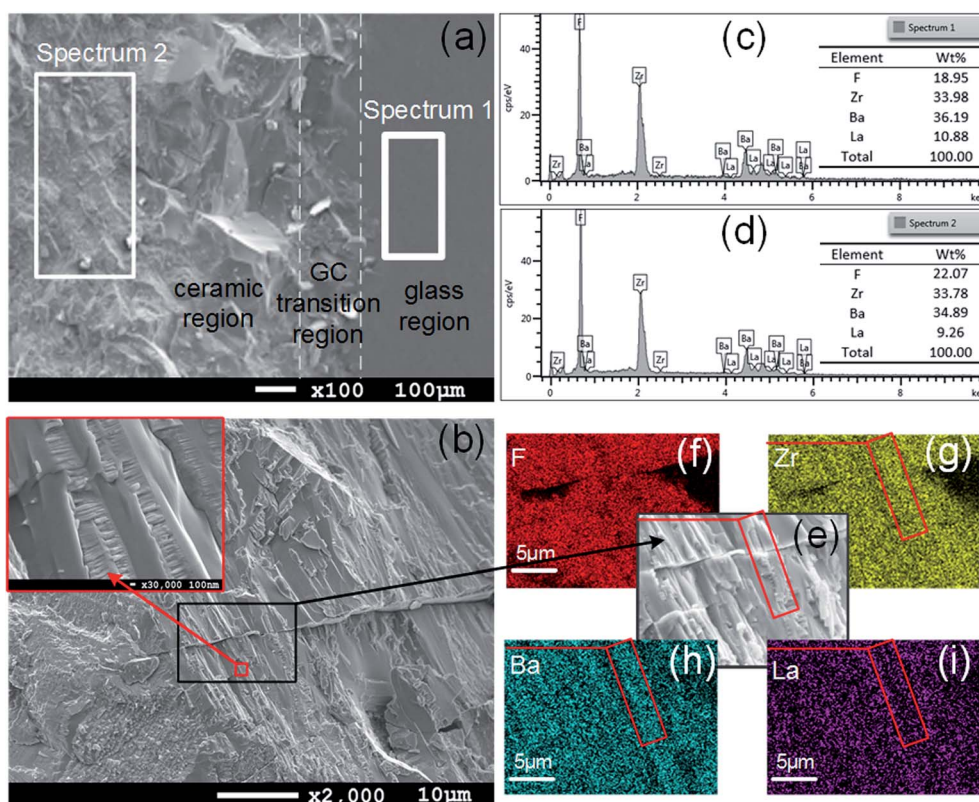


Fig. 4 (a and b) SEM images of the cross-section of GC_{ZBL}-Eu. (c and d) EDS spectra and the elemental content of G_{ZBL}-Eu and C_{ZBL}-Eu. (e–i) Elemental mapping of C_{ZBL}-Eu.



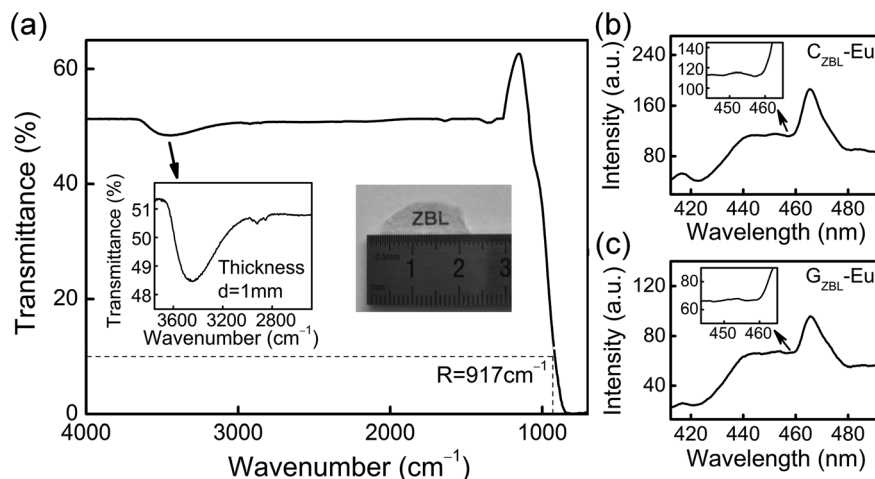


Fig. 5 (a) The FT-IR spectrum of the glass layer. (b and c) The excitation spectra of $G_{ZBL}\text{-Eu}$ and $C_{ZBL}\text{-Eu}$ monitored at 615 nm emission.

order to maintain electrical neutrality, Eu^{3+} , whose radius of 0.95 Å is between that of Zr^{4+} (0.80 Å) and Ba^{2+} (1.35 Å), is more likely to replace Zr^{4+} in the lattice and forms F^- vacancies.

Molten glass appears to be disordered owing to increased interatomic amplitudes and irregular diffusion of the molecules, and the disordered state is fixed to form a glass on sudden cooling. When molten glass cools down slowly, each atom returns to the lowest energy state and forms crystals. In this matrix, BaZrF_6 is a crystal with lower lattice energy and is easier to precipitate; Fig. 3 shows the schematic diagram of the crystal structure of BaZrF_6 .

Spectrum 1 and spectrum 2 with the same element type were chosen from the SEM images of the sample cross-section in Fig. 4(a) for elemental analysis, as shown in Fig. 4(c) and (d). In comparison, the element contents in $G_{ZBL}\text{-Eu}$ and $C_{ZBL}\text{-Eu}$ have little difference within the allowable error range, indicating that there is no obvious element migration during the crystallization process. In addition, the absence of oxygen and other elements in the EDS spectra indicates that there is no foreign matter in the prepared $G_{ZBL}\text{-Eu}$ and $C_{ZBL}\text{-Eu}$ and the surface of the samples is not oxidized. The SEM image of the ceramic region displays that the BaZrF_6 crystalline grain covered by glass in

$C_{ZBL}\text{-Eu}$ grows in an ordered direction and arrangement, as shown in Fig. 4(b). The elemental mapping in the regions contained within the red frames of Fig. 4(e–i) exhibits that Zr and Ba are densely distributed whereas it is the opposite for La, which indicates that the red frame region represents the cross-section of the BaZrF_6 grains coated with glass.

Based on the FT-IR spectrum of the glass layer in Fig. 5(a), the molar absorption coefficient α_{OH} can be used to evaluate the residual OH content in the glass samples and was found to be 0.91 cm^{-1} in the $75\text{TeO}_2\text{-}10\text{ZnO-}10\text{Na}_2\text{O-}5\text{GeO}_2$ glasses,²⁶ while the value in this work is as low as 0.57 cm^{-1} . The low OH content of the samples is helpful in achieving the anticipated photon emission by reducing the fluorescence loss. In view of the high sensitivity of the multi-channel transition to the phonon energy, the maximum phonon energy (E) of the glass samples was estimated through the empirical formula $E = 92.9 + 0.4257R$, where R corresponds to the wavenumber at 10% transmittance of the infrared transmission sideband and the maximum phonon energy of $G_{ZBL}\text{-Eu}$ is identified to be $\sim 483 \text{ cm}^{-1}$.

The energy difference between the phonon sideband spectrum and the zero-phonon line is the coupled phonon energy

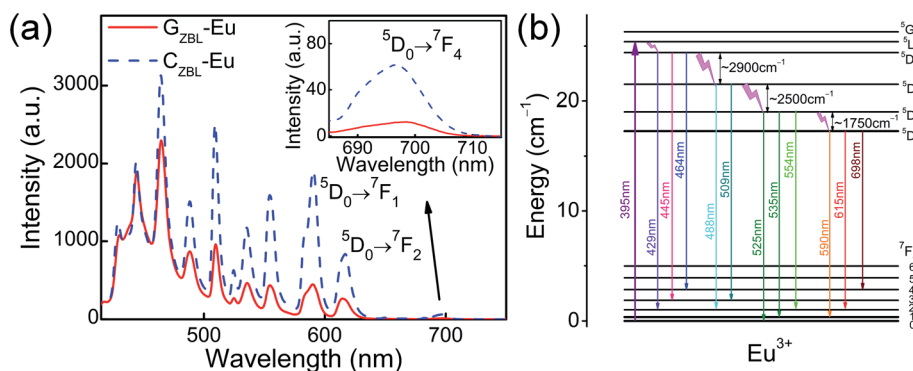


Fig. 6 (a) Emission spectra of $G_{ZBL}\text{-Eu}$ and $C_{ZBL}\text{-Eu}$ under 395 nm excitation. (b) The schematic diagram of multimodal emission energy levels of Eu^{3+} under 395 nm excitation.



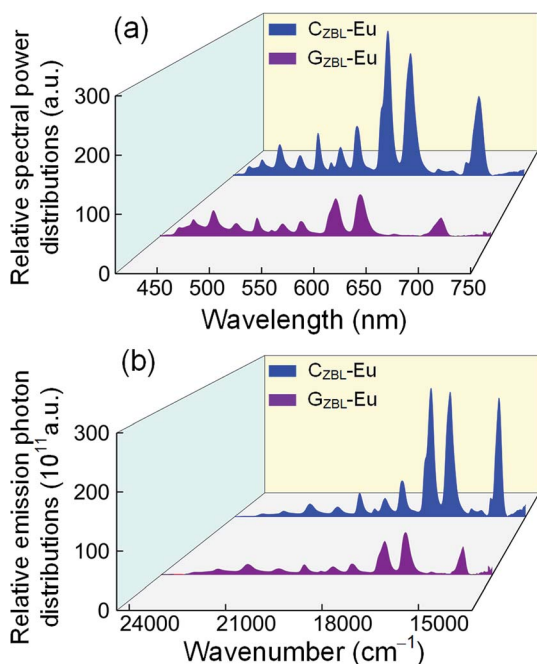


Fig. 7 The relative spectral power distributions (a) and the relative emission photon distributions (b) of GZBL-Eu and CZBL-Eu under 395 nm excitation.

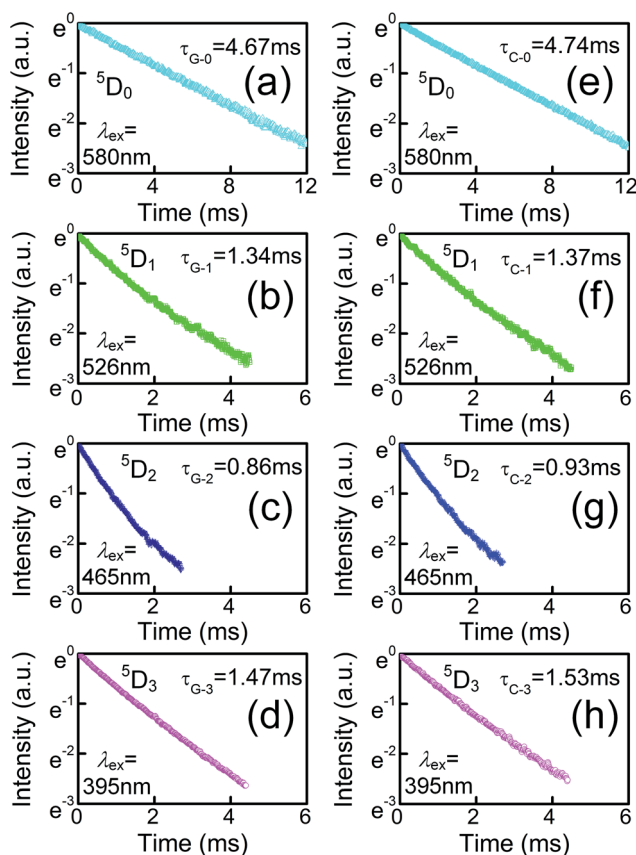


Fig. 8 Fluorescence decay curves from the 5D_0 , 5D_1 , 5D_2 , and 5D_3 level of Eu^{3+} in GZBL-Eu (a–d) and CZBL-Eu (e–h) monitored at 615, 535, 509, and 464 nm, respectively.

for the electron transition of the RE^{3+} ions. The phonon energies of GZBL-Eu and CZBL-Eu were estimated to ~ 452 and $\sim 424\text{ cm}^{-1}$ according to the fitting of the two curves shown in Fig. 5(b) and (c), respectively. The local vibrational modes with the corresponding RE^{3+} ions are generally considered to be slightly less than the maximum phonon energy of the material.²⁷ GZBL-Eu and CZBL-Eu with low phonon energies, which have been confirmed by the two methods mutually, can reduce the possibility of non-radiative transitions and facilitate fluorescence emission.

The emission spectra of GZBL-Eu and CZBL-Eu were recorded under 395 nm excitation as shown in Fig. 6(a). The emission intensity of CZBL-Eu is much higher than that of GZBL-Eu owing to the ordered arrangement of BaZrF_6 particles and another factor is that Eu^{3+} maybe be retained in CZBL-Eu more than in GZBL-Eu. Eleven emission peaks of GZBL-Eu and CZBL-Eu are located at 429, 445, 464, 488, 509, 525, 535, 554, 590, 615, and 698 nm, which originate from the $^5D_3 \rightarrow ^7F_{2,3,4}$, $^5D_2 \rightarrow ^7F_{2,3}$, $^5D_1 \rightarrow ^7F_{0,1,2}$, and $^5D_0 \rightarrow ^7F_{1,2,4}$ transitions of Eu^{3+} , respectively. The energy level diagram in Fig. 6(b) shows the radiation and relaxation processes of multiple channels and the values of energy gaps among the 5D_0 , 5D_1 , 5D_2 , and 5D_3 levels. In the GZBL-Eu and CZBL-Eu systems, the multiphonon relaxation processes from the 5D_3 and 5D_2 levels are accomplished by six-phonon bridging and that from 5D_1 level is completed by four-phonon bridging. All of them belong to high order processes (more than 3 phonons) and thus, the probability of energy loss by non-radiative transitions is lowered. Therefore, the blue and green light emission peaks from 5D_3 , 5D_2 , and 5D_1 levels cooperating with the red-light emission peaks from the 5D_0 level can be well applied to luminescent color tuning, thus expanding the application direction of single RE^{3+} ions.

By referring to the halogen lamp, the relative spectral power distribution is converted from the emission spectrum and is shown in Fig. 7(a). Depending on the relative spectral power distribution, photon distribution $N(\nu)$ can be deduced as $N(\nu) = \frac{\lambda^3}{hc} P(\lambda)$, where ν , λ , h , c , and $P(\lambda)$ represent the wave-number, wavelength, Planck constant, vacuum light velocity, and spectral power distribution, respectively.^{28–30} Under 395 nm excitation, the emission photon number distribution curves of GZBL-Eu and CZBL-Eu are derived as shown in Fig. 7(b).

Ω_2 , which is influenced by the local structure symmetry of Eu^{3+} in GZBL-Eu and CZBL-Eu, is usually used to describe the emission distribution of the 5D_0 level and can be calculated based on the emission photon number distributions instead of the general absorption spectra. In the calculation, the ordinary refractive index n value of GZBL-Eu is measured to be 1.555 and the value of CZBL-Eu is estimated to be 1.590.³¹ The Ω_2 value of Eu^{3+} in CZBL-Eu is $1.75 \times 10^{-20}\text{ cm}^2$, which is lower than $2.49 \times 10^{-20}\text{ cm}^2$ in GZBL-Eu. A smaller Ω_2 value indicates a higher symmetry of the local structure of Eu^{3+} ions and weaker covalency around the metal–donor interaction. Also, compared with CZBL-Eu, GZBL-Eu, and other substrates,^{32–37} a smaller Ω_2 value (higher symmetry) corresponds to lower red-light emission ratio of the $^5D_0 \rightarrow ^7F_2$ transition. In other words, at a higher symmetry site, the intensity ratio of the $^5D_0 \rightarrow ^7F_2$ emission is reduced and thus,

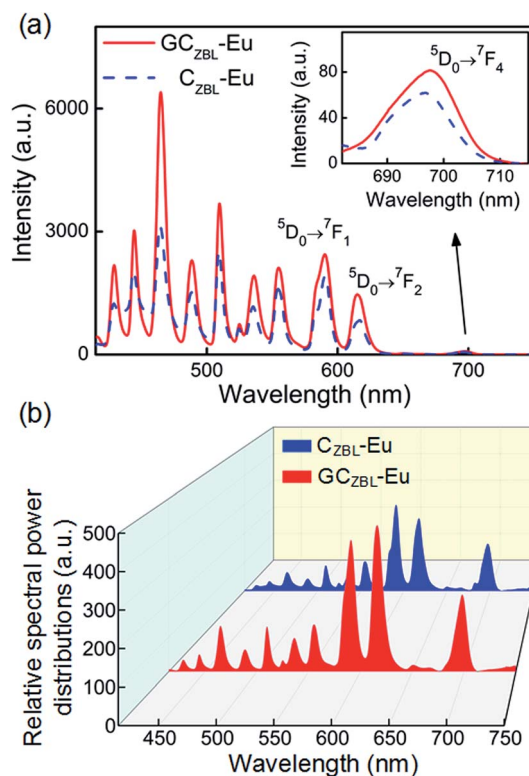


Table 1 The experimental lifetimes and de-population rates of 5D_0 , 5D_1 , 5D_2 , and 5D_3 in G_{ZBL} -Eu and C_{ZBL} -Eu

Energy level	G_{ZBL} -Eu		C_{ZBL} -Eu	
	Experimental lifetime (ms)	De-population rate (s^{-1})	Experimental lifetime (ms)	De-population rate (s^{-1})
5D_0	4.67	214	4.74	211
5D_1	1.34	746	1.37	730
5D_2	0.86	1163	0.93	1075
5D_3	1.47	680	1.53	654

it becomes more similar to that of the $^5D_0 \rightarrow ^7F_1$ transition. This means that C_{ZBL} -Eu can better limit the emission of red light and using the shorter-wavelength orange light generated in the $^5D_0 \rightarrow ^7F_1$ transition, it is easier to synthesize white light with blue and green light from the 5D_3 , 5D_2 , and 5D_1 level transitions. Such a change towards more equal intensity emission at various wavelengths is more suitable for realizing an overall white emission of the phosphor and the excitation source system.

To better express the capacity of the potential radiative transition among the levels, the experimental average lifetimes and the de-population rate of Eu^{3+} in G_{ZBL} -Eu and C_{ZBL} -Eu can be derived from the fluorescence decay curves, as shown in Fig. 8, and the related results are calculated and listed in Table 1. In the fluoride system with low phonon energy, photons can be effectively released and the low de-population rate represents that the radiative transition occupies a major proportion. In order to evaluate the effective radiation of C_{ZBL} -Eu and G_{ZBL} -Eu, the quantum efficiencies of the 5D_0 level was calculated. The data of theoretical radiative fluorescent lifetimes (including the relevant calculation data), experimental average lifetimes, and quantum efficiencies are listed in Table 2. The quantum efficiencies of Eu^{3+} from the 5D_0 level in G_{ZBL} -Eu and C_{ZBL} -Eu were calculated to be 98.5% and 94.8%, which demonstrate the effectiveness of radiative transition emission from Eu^{3+} in G_{ZBL} -Eu and C_{ZBL} -Eu. The difference in the quantum efficiencies of G_{ZBL} -Eu and C_{ZBL} -Eu is consistent with the conclusion that the luminous efficiency of Eu^{3+} decreases in a more symmetrical crystal field environment. The high quantum efficiencies of G_{ZBL} -Eu and C_{ZBL} -Eu demonstrate the effectiveness of radiative transition emissions from Eu^{3+} and show the application prospects in energy conversion and energy saving.

**Fig. 9** Comparison of emission intensities (a) and the relative spectral power distributions (b) between C_{ZBL} -Eu and GC_{ZBL} -Eu under 395 nm excitation.

The emission spectra and the relative spectral power distributions of C_{ZBL} -Eu and GC_{ZBL} -Eu are shown in Fig. 9(a) and (b) under 395 nm excitation, and both them show multi-channel

Table 2 Photon number ratios, spontaneous transition probabilities A_{ij} , fluorescence branching ratios β_{ij} , calculated radiative fluorescent lifetimes τ_{rad} , experimental average lifetimes τ_{exp} , and quantum efficiencies of 5D_0 in G_{ZBL} -Eu and C_{ZBL} -Eu

Sample	Transition	Energy (cm^{-1})	Photon number ratio	A_{ij} (s^{-1})	β_{ij} (%)	τ_{rad} (ms)	τ_{exp} (ms)	Quantum efficiency (%)
G_{ZBL} -Eu	$^5D_0 \rightarrow ^7F_1 (N_1)$	16 949	—	64.3	30.5	4.74	4.67	98.5
	$^5D_0 \rightarrow ^7F_2 (N_2)$	16 271	$N_2/N_1 = 1.30$	83.8	39.7			
	$^5D_0 \rightarrow ^7F_4 (N_4)$	14 318	$N_4/N_1 = 0.98$	63.0	29.8			
	$^5D_0 \rightarrow ^7F_1 (N_1)$	16 938	—	68.7	34.4			
C_{ZBL} -Eu	$^5D_0 \rightarrow ^7F_2 (N_2)$	16 207	$N_2/N_1 = 0.98$	63.3	31.7	5.00	4.74	94.8
	$^5D_0 \rightarrow ^7F_4 (N_4)$	14 351	$N_4/N_1 = 1.06$	67.9	33.9			
	$^5D_0 \rightarrow ^7F_1 (N_1)$	16 938	—	68.7	34.4			



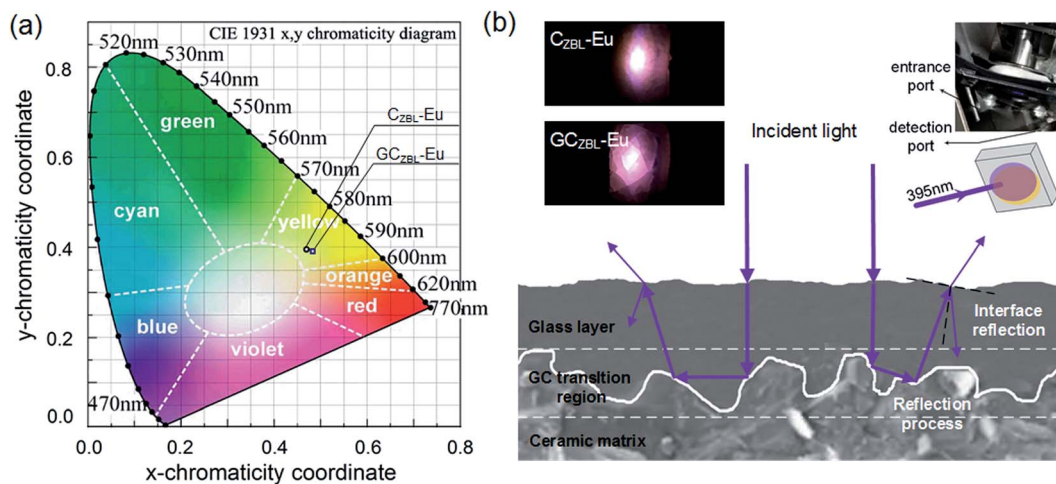


Fig. 10 (a) Color coordinates in the CIE 1931 chromaticity diagram of $C_{ZBL}\text{-Eu}$ and $GC_{ZBL}\text{-Eu}$ under 395 nm excitation. (b) The schematic diagram of enhanced $GC_{ZBL}\text{-Eu}$ emission process under 395 nm excitation. Inset: fluorescent photographs of $C_{ZBL}\text{-Eu}$ and $GC_{ZBL}\text{-Eu}$ under 395 nm excitation (left), and the schematic of the photos obtained (right).

radiative transitions of Eu^{3+} in $C_{ZBL}\text{-Eu}$ and $GC_{ZBL}\text{-Eu}$. Herein, the CIE-1931 chromaticity coordinates for the luminescence of $C_{ZBL}\text{-Eu}$ and $GC_{ZBL}\text{-Eu}$ were derived to be (0.483, 0.385) and (0.469, 0.389), which fall into the yellowish-white region, as shown in Fig. 10(a). The chromaticity coordinates prove that the emission light of $C_{ZBL}\text{-Eu}$ and $GC_{ZBL}\text{-Eu}$ is yellowish-white, suggesting that the Eu^{3+} -activated $GC_{ZBL}\text{-Eu}$ system has application prospect as a single phosphor.

The emission intensity of $GC_{ZBL}\text{-Eu}$ at 590 nm is 1.24 times higher than that for $C_{ZBL}\text{-Eu}$, where the significant improvement in the emission intensity can be attributed to the complex surface morphology of the ceramic matrix and the intense dispersion effect of the glass layer, and the schematic diagram of increasing the incident light absorption efficiency and enhancing the emission is shown in Fig. 10(b). When the incident light shines into $GC_{ZBL}\text{-Eu}$, the under-utilized light is re-reflected to the ceramic boundary, forming a multiple-cycle reflection effect owing to the specular reflection of the glass layer. Then, the incident light will be absorbed by the glass phase in the reflection process of the glass–ceramic transition region and is converted into other wavelengths for emission.

As shown in the inset of Fig. 10(b), intense lighting is observed in $C_{ZBL}\text{-Eu}$ and $GC_{ZBL}\text{-Eu}$, and the violet lighting in the picture is illuminated by a 395 nm Xe lamp. Simultaneously, the purple source overlaps with the emitted yellowish-white light to form the pink-white light. Effective fluorescence emission enhancement facilitates better application of $GC_{ZBL}\text{-Eu}$ with warm-white light emission of laser lighting.

Conclusion

Hetero-structured $GC_{ZBL}\text{-Eu}$ with glass region, ceramic region, and GC transition region obtained by the one-step method exhibits yellowish-white light and the crystal phase of $C_{ZBL}\text{-Eu}$ is identified as BaZrF_6 . Multi-channel radiative transitions were discovered through multi-peak emission, long fluorescence lifetimes, and de-population rates of the 5D_0 , 5D_1 , 5D_2 , and 5D_3

levels in $G_{ZBL}\text{-Eu}$ and $C_{ZBL}\text{-Eu}$, which is because the low OH content and low phonon energy limit the non-radiative relaxation. The effective radiative transition emission of the 5D_0 levels in $G_{ZBL}\text{-Eu}$ and $C_{ZBL}\text{-Eu}$ is demonstrated by the high quantum efficiency of 98.5% and 94.8%, respectively. The release of yellowish-white light is indicated by the color coordinates of $C_{ZBL}\text{-Eu}$ (0.483, 0.385) and $GC_{ZBL}\text{-Eu}$ (0.469, 0.389), and the emission intensity of $GC_{ZBL}\text{-Eu}$ is 1.24 times higher than that of $C_{ZBL}\text{-Eu}$ due to multiple-cycle reflection in the complex structure of the GC transition region. The effective yellowish-white lighting proves that the $GC_{ZBL}\text{-Eu}$ system with fluorescence enhancement has potential in the application direction of laser illumination.

Conflicts of interest

There are no conflicts to declare.

Acknowledgements

The research work was supported by the Scientific Research Funding Project from the Educational Department of Liaoning Province, China (Grant No. J2019021) and the Research Grants Council of the Hong Kong Special Administrative Region, China (Grant No. CityU 11218018).

References

- 1 T. Mondal, S. Mondal, S. Bose, D. Sengupta, U. K. Ghorai and S. K. Saha, *J. Mater. Chem. C*, 2018, **6**, 614–621.
- 2 C. Y. Sun, X. L. Wang, X. Zhang, C. Qin, P. Li, Z. M. Su, D. X. Zhu, G. G. Shan, K. Z. Shao, H. Wu and J. Li, *Nat. Commun.*, 2013, **4**, 2717.
- 3 Q. Wang and D. Ma, *Chem. Soc. Rev.*, 2010, **39**, 2387–2398.
- 4 X. Q. Liao, X. Yang, R. Zhang, J. Cheng, J. Li, S. Y. Chen, J. Zhu and L. Li, *J. Mater. Chem. C*, 2017, **5**, 10001–10006.



- 5 H. Li, H. B. Liu, X. M. Tao, J. Su, P. F. Ning, X. F. Xu, Y. Zhou, W. Gu and X. Liu, *J. Mater. Sci.*, 2014, **49**, 4439–4444.
- 6 Z. Gao, S. Liu, P. Sun, J. H. Jeong, R. Yu and B. Deng, *J. Rare Earths*, 2018, **36**, 917–923.
- 7 M. Mazzeo, V. Vitale, F. Della Sala, M. Anni, G. Barbarella, L. Favaretto, G. Sotgiu, R. Cingolani and G. Gigli, *Adv. Mater.*, 2005, **17**, 34–39.
- 8 R. S. Deshpande, V. Bulović and S. R. Forrest, *Appl. Phys. Lett.*, 1999, **75**, 888–890.
- 9 H. P. Barbosa, I. G. N. Silva, M. C. F. C. Felinto, E. E. S. Teotonio and H. F. Brito, *J. Alloys Compd.*, 2017, **696**, 820–827.
- 10 N. Guo, Y. Huang, H. You, M. Yang, Y. Song, K. Liu and Y. Zheng, *Inorg. Chem.*, 2010, **49**, 10907–10913.
- 11 P. Y. Poma, W. Q. Santos, T. O. Sales, A. S. Gouveia-Neto and C. Jacinto, *J. Lumin.*, 2017, **188**, 18–23.
- 12 S. A. Ying, S. Xiao, J. W. Yao, Y. F. Dai, D. Z. Yang, X. F. Qiao, J. S. Chen, T. F. Zhu and D. G. Ma, *Adv. Opt. Mater.*, 2019, **7**, 1901291.
- 13 X. Liu, Y. Li, T. Aidilibike, J. Guo, W. Di and W. Qin, *J. Lumin.*, 2017, **185**, 247–250.
- 14 L. Han, S. Xie, M. Wang, T. Sun, Q. Liu, G. Jiang, Y. Shi and Y. Tang, *Mater. Lett.*, 2019, **234**, 241–244.
- 15 Y. Yu, D. Chen, P. Huang, H. Lin and Y. Wang, *Ceram. Int.*, 2010, **36**, 1091–1094.
- 16 A. Balamurugan, M. L. Reddy and M. Jayakannan, *J. Mater. Chem. A*, 2013, **1**, 2256–2266.
- 17 J. N. Hao and B. Yan, *J. Mater. Chem. A*, 2014, **2**, 18018–18025.
- 18 X. Shen and B. Yan, *J. Mater. Chem. C*, 2015, **3**, 7038–7044.
- 19 J. J. Velázquez, J. Mosa, G. Gorni, R. Balda, J. Fernández, A. Durán and Y. Castro, *J. Non-Cryst. Solids*, 2019, **520**, 119447.
- 20 X. Liu, J. Zhou, S. Zhou, Y. Yue and J. Qiu, *Prog. Mater. Sci.*, 2018, **97**, 38–96.
- 21 L. Li, H. K. Yang, B. K. Moon, Z. Fu, C. Guo, J. H. Jeong, S. S. Yi, K. Jang and H. S. Lee, *J. Phys. Chem. C*, 2008, **113**, 610–617.
- 22 B. Rajamouli, P. Sood, S. Giri, V. Krishnan and V. Sivakumar, *Eur. J. Inorg. Chem.*, 2016, **2016**, 3900–3911.
- 23 S. K. Gupta, M. Mohapatra, V. Natarajan and S. V. Godbole, *J. Mater. Sci.*, 2012, **47**, 3504–3515.
- 24 N. Wantana, E. Kaewnuam, B. Damdee, S. Kaewjaeng, S. Kothan, H. J. Kim and J. Kaewkhao, *J. Lumin.*, 2018, **194**, 75–81.
- 25 Y. Y. Li and S. Q. Xu, *RSC Adv.*, 2018, **8**, 31905–31910.
- 26 V. A. G. Rivera, M. El-Amraoui, Y. Ledemi, Y. Messaddeq and E. Marega Jr, *J. Lumin.*, 2014, **145**, 787–792.
- 27 S. Todoroki, K. Hirao and N. Soga, *J. Non-Cryst. Solids*, 1992, **143**, 46–51.
- 28 R. K. Pushpendra Kunchala, S. N. Achary and B. S. Naidu, *ACS Appl. Nano Mater.*, 2019, **2**, 5527–5537.
- 29 R. K. Pushpendra Kunchala, S. N. Achary, A. K. Tyagi and B. S. Naidu, *Cryst. Growth Des.*, 2019, **19**, 3379–3388.
- 30 B. S. Naidu, B. Vishwanadh, V. Sudarsan and R. K. Vatsa, *Dalton Trans.*, 2012, **41**, 3194–3203.
- 31 G. De Leede, R. Beerkens, E. Van Duin and H. De Waal, *J. Mater. Sci.*, 1992, **27**, 2309–2315.
- 32 N. Li, Y. Xue, D. Wang, B. Liu, C. Guo, Q. Song, X. Xu, J. Liu, D. Li, J. Xu, Z. Xu and J. Xu, *J. Lumin.*, 2019, **208**, 208–212.
- 33 M. Kaczkan, S. Turczyński and M. Malinowski, *J. Lumin.*, 2018, **196**, 111–115.
- 34 Y. Tian, B. Chen, R. Hua, N. Yu, B. Liu, J. Sun, L. Cheng, H. Zhong, X. Li, J. Zhang, B. Tian and H. Zhong, *Crystengcomm*, 2012, **14**, 1760–1769.
- 35 L. Liu and X. Chen, *Nanotechnology*, 2007, **18**, 255704.
- 36 P. A. Loiko, V. I. Dashkevich, S. N. Bagaev, V. A. Orlovich, X. Mateos, J. M. Serres, E. V. Vilejshikova, A. S. Yasukevich, K. V. Yumashev, N. V. Kuleshov, E. B. Dunina, A. A. Kornienko, S. M. Vatnik and A. A. Pavlyukf, *J. Lumin.*, 2015, **168**, 102–108.
- 37 P. Loiko, E. V. Vilejshikova, A. A. Volokitina, V. A. Trifonov, J. M. Serres, X. Mateos, N. V. Kuleshov, K. V. Yumashev, A. V. Baranov and A. A. Pavlyuk, *J. Lumin.*, 2017, **188**, 154–161.

